

Wireless Muometric Navigation System

Hiroyuki K.M. Tanaka (✉ ht@eri.u-tokyo.ac.jp)

University of Tokyo

Research Article

Keywords:

Posted Date: February 24th, 2022

DOI: <https://doi.org/10.21203/rs.3.rs-1348393/v1>

License:  This work is licensed under a Creative Commons Attribution 4.0 International License. [Read Full License](#)

Abstract

While satellite-based global navigation systems have become essential tools in our daily lives, their effectiveness is often hampered by the fact that the signals cannot be accessed in underground, indoor, or underwater environments. Recently, a novel navigation system has been invented to address this issue by utilizing the characteristics of the ubiquitous and highly penetrative cosmic-ray muons. This technique, muometric navigation, does not require active signal generation and enables positioning in the aforementioned environments within a reference coordinate defined by the three-dimensional positions of multiple detectors. In its first phase of development, these reference detectors had to be connected to the receivers via a wired configuration to guarantee precise time synchronization. This work describes more versatile, wireless muometric navigation system (MuWNS), which was designed in conjunction with a cost-effective, crystal-oscillator-based grandmaster clock and a performance evaluation is reported for shallow underground/indoor, deep underground and undersea environments. It was confirmed that MuWNS offers a navigation quality almost equivalent to aboveground GPS-based handheld navigation by determining the distance between the reference frame and the receivers within a precision range between 1 m and 10 m.

Introduction

In recent decades, Global Positioning System (GPS) or Global Navigation satellite system (GNSS) has become increasingly prominent, since transportation (aircrafts, boats, cars, and even excursions on foot) frequently relies on GPS for navigation and tracking, often from handheld devices. Wireless navigation, using a combination of GPS and portable receivers embedded in aircraft/boat/car navigation systems or smartphones, has supported transportation or directional orientation^{1,2,3,4}, checking patterns of human movement^{5,6,7}, and even health tracking^{8,9,10}. However, the range of GPS does not extend to underground/indoor and underwater environments, therefore in those regions, navigation capability is still quite limited. Currently, the most common methods to use for navigation in such environments are based on acoustic¹¹, Wi-Fi¹², cellphone signals¹³, Bluetooth low energy (e.g., iBeacon), Indoor messaging system (IMES)¹⁴, and ultrasonic techniques¹⁵. However, all of these systems need an active source; hence they require pre-installed infrastructures such as acoustic transmitters/transceivers, Wi-Fi access points and/or cell towers and/or iBeacon/IMES transmitters, and generally these high-cost resources are only available in highly populated areas. When these infrastructures are not available or only partially available, the positioning accuracy will be low. For example, although the cellphone-based navigation technique can be used for navigation in mountainous and underground environments as long as the cellphone signals are available, the positioning accuracy is limited to a few km to a few tens of kilometers¹⁶. On the other hand, the pedestrian dead reckoning (PDR)¹⁷ and barometric¹⁸ techniques are passive techniques and thus, these techniques don't require pre-installed infrastructure developments; however, since these techniques only measure the relative positions or can only determine the elevation information, generally these techniques have to be combined with other active techniques.

Recently, a novel passive navigation system using cosmic rays was invented¹⁹ as an underground and underwater navigation system, with the objective that it could also be applied to navigation at latitudes

where GPS works poorly²⁰. The technique is called the muometric navigation system or muometric positioning system (muPS) and utilizes the ubiquitous and penetrative nature of cosmic ray muons that have also been applied to muography to visualize interior structures of gigantic objects such as volcanoes and pyramids^{19,20,21,22,23,24,25,26,27,28,29,30,31,32}; when these naturally occurring probes are adapted for navigation, the receiver detector's position can be determined with centimeter-level accuracy within the coordinates defined by the reference detectors. In the first muPS demonstrations, the reference detectors and receiver detector were connected with wires for time synchronization, and thus the application range was limited. However, by using a wireless system to determine the position of the receivers, muPS can be more flexible and thus adaptable to a wider-range of applications. The time-to-digital-converter's (TDC's) sub-nanosecond jitter, measured in the range of microseconds, is much larger than the fluctuations in the muon's time of flight¹⁹ (TOF) and thus, both effects are negligible as long as the required positioning accuracy is in the order of meters. Therefore, the quality control of the time synchronization between the reference detectors and receiver detector is a key factor to realize the idea of wireless muPS.

GPS signals are one of the most common time synchronization signal inputs. Wireless devices can achieve perfect time alignment to coordinated universal time (UTC) by using GPS. However, this solution does not function in indoor, underground or underwater environments since GPS signals are not available in such environments. Another possibility to achieve good time alignment is the grandmaster clock's (GMC's) "holdover"³³ mode. Synchronization standards have defined the term "holdover" to refer to time synchronization that functions reliably even when the GPS synchronization input has been disrupted or temporarily unavailable. The holdover mode can be used for time synchronization between the reference and receiver detectors. Even without GPS signals, a holdover mode controlled by a high-quality oscillator keeps a high synchronization level, and an oven-controlled crystal oscillator (OCXO) has already been industrially produced to provide reliable and accurate holdover measurement. In this work, the design of a new wireless muPS that works in conjunction with this OCXO-based GMC's holdover mode will be presented and its performance will be evaluated.

Results

Principle. The principle of muPS is similar to that of GPS. The muPS uses, instead of satellites, three or more detectors to form the reference coordinate (Fig. 1). The receiver detector defines the relative position within this coordinate by using the following relationship:

$$L_i^2 = (x_i - x_p)^2 + (y_i - y_p)^2 + (z_i - z_p)^2, \quad (1)$$

where L_i is the geometrical distance between the i th reference detector located at (x_i, y_i, z_i) and the receiver detector located at (x_p, y_p, z_p) . Since the muon's traveling speed is approximately the speed of light in a vacuum (c_0)¹⁹, the distance (L_i) between the reference detector and the receiver detector is determined by the muon's time of flight (TOF) between them. If the clocks attached to the reference detectors (reference clocks) and those attached to the receiver detectors (receiver clocks) are synchronized, this TOF is defined by the difference of the muon's arrival time between the reference and receiver detectors. Since L_i , x_i , y_i and

z_i are known, Eq. (1) has three variables; hence a ternary operation of Eq. (1) with three independent muon tracks will suffice. However, when conducting navigation with wireless muometric navigation system (MuWNS), the time synchronization between the reference clocks and receiver clocks is not automatically guaranteed. Actually, the stand-alone clock attached to the receiver detector is more likely to have a time offset error (Δt) due to the frequency-drift of the crystal oscillators (OCXOs). Therefore, for MuWNS, Eq. (1) will have one more variable such that:

$$L_i^2 = (x_i - x_p)^2 + (y_i - y_p)^2 + (z_i - z_p)^2 + s^2, \quad (2)$$

where $s (= c_0 \Delta t)$ is the pseudo-length that comes from the time offset at the receiver detector. Consequently, one variable was added to Eq. (1) and thus, at least four reference detectors will always be required for MuWNS. The positioning scheme shown in Eq. (2) holds only when we can assume that the time offset (Δt) stays at the same constant rate or nearly constant rate within the time range required for positioning. The errors in determining L_i are defined as ΔL_i in this work. For simplicity, it was also assumed that the reference detectors were constantly connected to the GPS antenna and getting an uninterrupted signal.

Required accuracy for MuWNS. In order to evaluate what the most practical positioning precision will be for each given situation, referencing the accuracy of commonly used portable GPS receivers is useful since the studies reporting the accuracy of these kinds of GPS receivers are extensive. For example, von Watzdorf and Michahelles³⁴ reported that the average accuracy of location information ranged between 108 and 655 m with GPS enabled Apple iPhones, iPods, and iPads. Zandbergen³⁵ reported that the average horizontal position error of an iPhone was around 10 m, and Garnett and Stewart³⁶ found better precision for positioning with an iPhone 4S which was around 6.5 m. However, these varieties of the positioning accuracy depend on the environment (such as how dense the buildings and trees, or topography are) since large structures surrounding the GPS receiver can cause multipath errors. In this work, we define the following three positioning precision categories for practical muometric navigation: Very Precise Level (VPL), a precision better than 1 m ($\Delta L_i \leq 1$ m); Precise Level (PL), a precision better than 3 m ($\Delta L_i \leq 3$ m); and Usable Level (UL) a precision better than 10 m ($\Delta L_i \leq 10$ m). Positioning accuracy worse than UL will be defined as an unpractical level and will not be discussed in this work.

Design of MuWNS. Figure 2 shows the block diagram of the current MuWNS. The time of the MuWNS setup is defined by the GMC, and every MuWNS detector records absolute time information. The GMC is connected to the GPS antenna when GPS signals are available. When GPS signals are not available (for some reason such as multipath reception, GPS jamming and spoofing, system failures, diving underwater, moving underground, etc.), the GMC will automatically switch from the GPS mode to the holdover mode. The muPS signals (e.g. photomultiplier tube (PMT) outputs) are discriminated with the constant fraction discriminator (CFD) and the time difference from the GMC signal is measured with the TDC (Fig. 2A). When GPS signals are not available, the event-counter-coincidence (ECC) unit starts to count the GMC signals at a rate of 10 MHz. When the GMC and muPS coincidence signals are generated, the number of GMC counts (n) and the timing information (t) are transferred to a microcomputer (e.g., Raspberry Pi) respectively from ECC and TDC. The transferred n and t values are shared between MuWNS detectors via Wi-Fi or an acoustic

modem to calculate the TOF. As a consequence, each MuWNS detector records the muon arrival time in a sharable form: $nT + t$, where T is the GMC/holdover signal period, and the "time zero" is defined as the moment when the GPS signal is lost (Fig. 2B); hence the TOF between the reference detector and the receiver detector can be derived by comparing reference and receiver clocks: $|[nT + t]_{\text{REFERENCE}} - [nT + t]_{\text{RECEIVER}}|$. The TDC is designed to reset start signals if it doesn't receive a stop signal before the next start signal, and the TDC time range must be sufficiently longer than T (in this case 100 ns). According to Tanaka (2020)¹⁹, since the jitter level for t is less than 200 ps, fluctuations in T will be a major factor to degrade the current TOF measurement quality. The errors in T will be described in the following subsections.

Grandmaster clock stability. The Grandmaster clock (GMC) stability is the key component to define the accuracy of MuWNS. Experimental results of the current GMC/holdover are described here. The timing jitter measured with the current GMC is shown in Fig. 3. These time-dependent variation plots were drawn in the following way. The OCXO used in the current work (Trimble OCXO) was equipped inside the GPS grandmaster clock (Trimble Thunderbolt PTP GM200). In this study, the Trimble OCXO was initially synchronized with the GPS signal by connecting a GPS antenna (See Method section). The OCXO was then subsequently disconnected to simulate indoor/underground/underwater navigation. This process was repeated 12 times to investigate the drift pattern. The results showed that the drift speed varied in each run, and both positive and negative drifts were measured. If the OCXO operation time lasted less than 1 hour, the drift was roughly linear as a function of time, but during longer operations, the behavior was unpredictable. Figure 3 shows the averaged time offset (the deviation between the GPS and holdover mode averaged over the entire run: $\langle \Delta t(t) \rangle$) and the standard deviation (SD) of $\Delta t(\sigma(t))$ as a function of time. Since both the drift speed and the drift direction were unpredictable, $\sigma(t)$ will remain as a non-zero factor. In MuWNS operations, Δt can be derived by solving Eq. (2), but non-zero σ will lead a major positioning error.

Time synchronization between reference clocks and underground/underwater clocks. In order to evaluate the time synchronization capability in Eq. (2) between the reference and receiver detectors with the currently designed MuWNS, the relationship between the GMC stability and the muon tracking frequency were studied. If the muon tracking frequency was too low, the uncertainties in the drift level and direction would increase, and $\sigma(t)$ would not be negligible, and as a consequence, quartic equations in Eq. (2) cannot be approximated as simultaneous equations anymore.

The muon's tracking frequency (N^{-1}) can be derived by integrating the open-sky zenith angular muon's energy spectrum $I(E, \theta)$ ^{37,38,39} over the energy range between E_c and infinity:

$$N(\theta) = \int_{E_c}^{\infty} I(E, \theta) dE, \quad (3)$$

where E, θ, φ are respectively the muon energy, elevation angle, and azimuth angle. E_c is the muon cutoff energy that depends on azimuthal variations of matter thickness located above the detector. For a derivation of E_c the muon's constant slowing down approximation (CSDA)⁴⁰ can be used. In order to keep the relativistic energy of muons in a state sufficiently higher than their invariant mass, E_c in Eq. (3) was set

to be 1 GeV higher than the cutoff energy directly derived from the CSDA muon range. N in Eq. (3) is also a function of the solid angle (Ω) formed by the reference and receiver detectors. If the size of the detectors (S) is given, Ω depends on the distance between the reference and receiver detectors.

Required spatial density of the reference detector network and resultant navigation performance. In order to evaluate spatial density of reference detectors required for achieving a given level of navigation performance of the currently designed MuWNS, the positioning accuracy and the time required for attaining this accuracy were studied. Generally, in the scheme of muPS, recording more muon tracks will improve the positioning accuracy more since the muon's arrival positions to the detector would be better averaged over the detection area, thus more muon events provide better positioning precision¹⁹. In the MuWNS scheme, the positioning errors coming from SD of Δt have to be considered in addition to the positioning errors coming from this detector size effect. Since σ increases as time goes by, the muon's tracking frequency and the positioning accuracy is tradeoff. In the following discussion, we assume the detector size is negligible in comparison to ΔL_i ; hence $\Delta L_i = c_0\sigma(t)$.

Figure 4 shows $c_0\sigma(t)$ as a function of the maximum distance between the reference and receiver detectors, where the maximum distance was defined as the distance (i.e., $S\Omega$) that enables each pair of the reference and receiver detectors to record at least one muon track within the given time so that $c_0\sigma(t)$ is less than the given accuracy level. In other words, if the distance between the reference and the receiver detectors exceeds this maximum distance, the given positioning accuracy will not be attainable due to the limited flux of cosmic-ray muons. Therefore, the maximum distance defines the required density of the receiver detectors for the required positioning precision. In this calculation, the effective active area of the reference and receiver detectors were both assumed to be 1 m², and a typical basement floor without surface structures above it was assumed; namely, the assumed characteristics were: 5-m thick soil (SiO₂) with an average density of 2.0 g cm⁻³ existing between the reference and the receiver detectors. As the muon's arrival angles approach the horizontal angle, the flux is reduced. As a consequence, the distance between the reference and receiver detectors has to be shortened to attain larger Ω . In this case, it is necessary to place reference detectors more densely.

Although the OCXO's frequency drift depends on a complicated combination of the environmental factors, it was expected that the resultant $\sigma(t)$ would be suppressed if we utilize multiple independent OCXOs and take an average of $\sigma(t)$ between them. Figure 5 compares $\sigma(t)$ averaged over single, double and triple OCXO outputs. For example, if we use three OCXOs, the time we are allowed to keep the low drift level to attain VPL will be extended from less than 9 seconds to less than 28 seconds. As a result, a less dense reference detector array will be required for a multiple OCXO system.

Discussion

The GMC with a Cs-oscillator-based holdover guarantees an order of magnitude higher stability than the OCXO-based holdover. However, OCXOs, which cost a hundred to a few hundred US dollars (USD), are far less expensive than atomic clocks that cost hundreds of thousand dollars. The current study clarified that

the MuWNS can operate with realistic logistics at reasonable costs. In this section, we will investigate possible MuWNS deployment scenarios in actual underground and undersea environments as example model cases. In the following case studies, the time required to go to the underground and underwater environments was neglected for the sake of simplicity.

Shallow underground. The geometrical configuration of the first example case is shown in Fig. 6. In this case, the Toranomon Hills Station Tower (THST) complex, a structure that will soon be built integrally with the subway station (Toranomon Hills Station) on the Tokyo Metro Hibiya line, was chosen as an example. THST was designed as a 51-story (49 above ground floors and 2 basement floors) building that accommodates a hotel and offices that directly connects to the subway station via an underground shopping center. For the current evaluation, two locations were chosen in this complex: (A) right underneath the THST and (B) at the Toranomon Hills Station (Figs. 6A and 6B). The underground space and the THST were modeled using empty voxel finite elements (0.0 gcm^{-3}) each measuring $10 \times 10 \times 10 \text{ m}^3$. The area surrounded by the red lines is used for the underground space, and the size of this area measures $14,300 \text{ m}^2$. In the THST region, it was assumed that the floor slabs with a thickness and density respectively of 30 cm and 2.0 gcm^{-3} were vertically spaced every 4.4 m. The density of the soil/basement floors was also assumed to be 2.0 gcm^{-3} . The thicknesses of the basement floors match the values shown in Fig. 6A, and the receiver was assumed to be located on B2F (at a depth of 15 m).

Figures 6C and 6D shows the azimuthal distribution of the soil/concrete thickness at Locations A and B. Location A is located right underneath the skyscraper. At Location A, by integrating Eq. (3) over the entire azimuthal range for different elevation angles, we found that this skyscraper effect was only effective above elevation angles larger than 40° (ranging 10%-70% of the open-sky flux for 40° - 90° from horizon). Below 40° , the soil thickness is as much as 10 m. At Location B, the THST effect was even weaker since only the westward component of the muon flux was affected by this building. Instead, the eastward component of the muon flux was more affected by the solid soil. Below 40° at Location B, the soil thickness was more than 40 m and thus, the muon flux arriving from this direction was reduced by 50%. Since the soil/concrete thickness was less than 10 m in the angular region below 40° , except for the edge of the underground space (red lines in Fig. 6B), the relationship shown in Fig. 4 can be directly applicable to this case. In conclusion, in order to attain VPL and PL, the reference detectors had to be located at an interval of 25 m and 50 m, respectively. These spatial densities respectively require aboveground 23 reference detectors and 6 reference detectors to cover the current complex area of $14,300 \text{ m}^2$. The cost required for developing MuWNS in this case will be discussed later. With this geometrical configuration, the times required to attain VPL and PL are respectively 28 seconds and 176 seconds. Here in this discussion MuWNS with triple OCXO (Fig. 5) was assumed. These time resolutions improve in proportion to the aperture size of the reference or receiver detectors. While it would be unrealistic for a pedestrian to carry a 1 m^2 detector as a handheld navigation system, the purpose of the current discussion is to model MuWNS operations in shallow underground/indoor environments. To adapt this system for handheld pedestrian navigation devices, several receiver detectors fixed to the basement floor could be combined with Wi-Fi or Bluetooth to view on smartphones.

Deep underground. The geometrical configuration of the second example case is shown in Fig. 7. In this case, Akiyoshido cave, Japan was chosen as an example. Akiyoshido cave is a limestone cave located underneath Akiyoshidai plateau, one of the largest karst plateaus in Japan, stretching over a total area of 54 square kilometers. The cave extends around 10 km lengthwise with ceilings reaching up to 80 m high. The tourist route is limited to regions approximately in a 1 km radius from the entrance. The Akiyoshidai area is well developed as a tourist's site; roads, cafes, museums, and observatories have been constructed above the cave. Therefore, it was relatively simple to design the experiment with realistic logistics.

As can be seen in Fig. 7, since the rock thickness situated between the reference and receiver detectors was much thicker than the first case (shown in Fig. 6), the size of the detector had to be larger. However, since it is unrealistic to enlarge the reference detector, it was assumed that a much larger reference detector with a detection area of $12 \times 2.5 \text{ m}^2$ was hypothetically installed in a 40-foot (12 m) standard freight container. Container trailers as large as 53 feet (15.9 m) could be rented, but since this 53-foot size is one of the largest sizes categorized for modern shipping, so we have chosen more common 40-foot container size since this is smaller and more convenient for standard truck-borne application. In this scheme, the reference detectors are mobile. In other words, the number of receiver detectors can be reduced if the total operation period doesn't exceed the time required for attaining a given positioning precision level since these can be moved. Figures 7A and 7B respectively show the side view and the photograph of the cave, and Figs. 7C, 7D and 7E show the possible positions of the tracks on the road or parking lots located above the cave. In this geometry, the overburden rock thicknesses range between 150 and 200 m, thus the viewing angle of the receiver detector was more or less than 1 msr, and the elevation angle between the receiver and reference detectors ranged between 300 and 500 mrad. Figure 8A shows the time required for recording one muon track as a function of rock thickness for various muon arrival angles from horizon. The number of reference detectors and the size of the receiver detector were respectively assumed to be four and $1.7 \times 1.7 \text{ m}^2$. Figure 8B shows the corresponding $c_0\sigma$. In this case, it was found that the current MuWNS setup was sufficient to achieve a UL level of navigation.

The digital Through-The-Earth (TTE) communication system can be used to provide communications links from the surface to below-ground locations. The system can be used to provide real-time monitoring of equipment sensors. The TTE communication uses very low frequency (VLF) transmission (transmission is usually done with magnetic induction, at frequencies below 30 kHz) to provide reliable data links through environments surrounded by rock, but in turn this system severely limits the bandwidth available for information transmission with data rates ranging from 9 bps to 1 kbps⁴¹. However, since both reference and receiver detectors have their own clock, the information that would have to be transferred to the counterpart detector to be effective is just n and t . Therefore, this data rate is sufficient for MuWNS communication requirements.

Undersea navigation. The geometrical configuration of the third example case is shown in Fig. 9A. In this case, a shallow bay (< 20 m) such as Tokyo Bay was chosen as an example, and a new scheme called the Robotic Vessels as-a-Service (RoboVaaS) was considered. RoboVaaS is a new scheme which intends to revolutionize shipping and near-shore operations in coastal waters by integrating and networking a smaller

Unmanned Surface Vehicle (USV) and an Unmanned Underwater Vehicle (UUV) efficiently in order to offer new services for shipping⁴². In this scheme, it was assumed that a number of USVs that carry reference detectors would navigate a number of UUVs operated at a depth of 15 m below sea level. The total size of the active area of the reference detector was assumed to be $20 \times 5 \text{ m}^2$, a size which could be easily accommodated on a small cargo boat. The size of the receiver detector was assumed to be $1.0 \times 1.0 \text{ m}^2$. It was also assumed that the positions of reference detectors can be defined in real time. Figure 9B shows the $c_0\sigma$ as a function of the muon arrival angles from the horizon. If we use more slanted muons, higher muon flux is available; hence the value of $c_0\sigma$ would be smaller for the given detector size and Ω , but a denser reference detector network would be needed. In order to plot this graph, E_c in Eq. (3) was derived from the CSDA muon range⁴⁰ for liquid H₂O with a density of 1.0 g cm^{-3} , and used for the lower limit of the integration process. The derived integrated flux was used for calculating the time required to record at least one muon track that passed through both a reference and a receiver detector. This time was converted to $c_0\sigma$ by using the $t-\sigma$ relationship shown in Fig. 5. As a consequence, it was found that the muon's arrival angle could be as low as 100 mrad and 175 mrad to achieve PL and VPL. These angles determine the USV network density required for attaining PL and VPL: 44 km^{-2} and 135 km^{-2} .

Cosmic Time Synchronizer. Fifth-generation (5G) mobile/cellular radio access network (RAN)⁴³, industrial automation and control systems⁴⁴, as well as land⁴⁵ and ocean⁴⁶ observation networks all require real-time connectivity with precise time synchronization to provide robust reference time information to the devices located in these networks on a common time basis with a jitter level below 1 microsecond⁴³. Such requirements are typically fulfilled through wired technologies like Time-sensitive Networking (TSN)⁴⁷. However, wireless technologies offer various benefits for network communication^{48,49}. MuWNS also offers a unique wireless time synchronization capability without GPS signal input, and the expected jitter level is less than 3.3 ns and less than 10 ns respectively for the VPL and PL mode. This means that if the reference detectors are receiving the GPS signals, the receiver detectors could get the absolute time in indoor, underground, or underwater environments.

Detector and operational costs. The MuWNS operational cost is very low. In the first case (Fig. 6), the required detectors are six 1-m^2 reference detectors and one 1-m^2 receiver detector for PL navigation. The cost of each 1-m^2 detector and photomultiplier tube (PMT) are respectively 5,000 USD and 1,000 USD. Therefore, the cost required for all these detectors will be 42,000 USD. Additionally, 2 GMCs and 2 TDCs will be required respectively for reference and receiver detectors, which will cost 10,000 USD. For multiple OCXO operations, development of the multiple OCXO GMCs will be needed since the current GMC only has one or two OCXOs, but it is expected that the adapted GMCs will not be so expensive since the cost of the OCXO is low (one hundred to a few hundred USD). In the second case (Fig. 7), much larger reference detectors are required. The required detector size is $2.5 \times 4 \text{ m}^2$ for each reference detector and 3-m^2 for receiver detector. The maximum length of one side of the reference detector is limited to 4 m due to the attenuation length of a high-quality scintillator. Therefore, the cost required for these detectors will be around 250,000 USD. In the third case (Fig. 9), ten $2.5 \times 4 \text{ m}^2$ reference detectors will be needed for each USV, thus, the required cost will be around 550,000 USD/USV. Even though the first investment costs are high in some cases, since MuWNS

is a passive navigation system, the power consumption is low; thus, the operational costs would be much lower in comparison to other active navigation systems.

In the current work, the GMC-holdover-based MuWNS was designed and evaluated its performance based on the GMC-OCXO data. Although the x-y-z positioning accuracy strongly depends on the geometric configuration of the reference and receiver detectors, we could conclude that the current MuWNS functions at a useful depth level in the shallow underground/indoor, deep underground and underwater. It is anticipated that MuWNS has the potential to become a practical and well-used new navigation system that could be applied to a variety of underground and underwater environments in the humanosphere (the regions of Earth utilized by and explored by humans) as a sustainable navigation system that doesn't require any active navigation signal generation.

Method

Experimental setup. In this demonstrational work, two independent GMCs (Trimble Thunderbolt PTP GM200) were used for evaluating the time synchronization capability between the aboveground/sea surface detectors and underground/underwater detectors. The GMC used for the time synchronization of the aboveground/sea surface detectors (aboveground GMC) was constantly connected to a GPS antenna to receive the time synchronization signal. The GMC used for the time synchronization of the underground/underwater detectors (underground GMC) was initially connected to a GPS antenna but then eventually disconnected. The GMC's PPS (pulse per second) signals were fed into the start and stop channels of a long time range (10 microseconds) TDC (Sciosence TDC-GPX) with a time resolution of 27 ps to measure the OCXO frequency drift as a time difference between the PPS pulses that were synchronized with the GPS clock and the PPS pulses that were generated by the OCXO without a frequency comparison with the GPS signals. Since both a positive (forward) and negative (delay) directional drift were expected, a delay circuit (600 ns) was inserted between the underground GMC and the TDC. The minimum receivable pulse width (10 ns) of the current TDC was sufficient for the measurement described here.

Declarations

Contributions

H.K.M.T. wrote the text. H.K.M.T. prepared the figures. H.K.M.T reviewed the manuscript.

Ethics declarations

Competing interests

The authors declare no competing interests.

References

1. Das, R. D. & Winter, S. A fuzzy logic based transport mode detection framework in urban environment. *J. Intelligent Trans. Syst.* **22**, 478–489 (2018).
2. Nour, A. *et al.* Classification of automobile and transit trips from smartphone data: Enhancing accuracy using spatial statistics and GIS. *J. Transp. Geogr.* **51**, 36–44 (2016).
3. Hofer, H. & Retscher, G. Seamless navigation using GNSS and Wi-Fi/IN with intelligent checkpoints. *J. Location Based Services* **11**, 204–221 (2017).
4. Vlahogianni, E. I. & Barmpounakis, E. N. Driving analytics using smartphones: Algorithms, comparisons and challenges. *Transp. Res. Part C Emerg. Technol.* **79**, 196–206 (2017).
5. Lue, G. & Miller, E. J. Estimating a Toronto pedestrian route choice mode using smartphone GPS data. *Travel Behav. and Soc.* **14**, 34–42 (2019).
6. Zhou, X. & Li, D. Quantifying multi-dimensional attributes of human activities at various geographic scales based on smartphone tracking. *Int. J. Health Geogr.* **17**, 29743069 (2018).
7. Glasgow, M. L. *et al.* Using smartphones to collect time-activity data for long-term personal level air pollution exposure. *J. Expo. Sci. Environ. Epidemiol.* **4**, 356–364 (2016).
8. Obuchi S. P. *et al.* Test-retest reliability of daily life gait speed as measured by smartphone global positioning systems. *Gait. Posture.* **61**, 282–286 (2018).
9. Hardy, J. *et al.* User acceptance of location-tracking technologies in health research: Implications for study design and data quality. *J. Biomed. Inform.* **79**, 7–19 (2018).
10. Aranki, D. *et al.* Real-time monitoring of patients with chronic heart-failure using a smartphone: Lessons learned. *IEEE Trans. Affect. Comput.* **7**, 206–219 (2016).
11. Kussat, N. H., Chadwell, C. D. & Zimmerman, R. Absolute positioning of an autonomous underwater vehicle using GPS and acoustic measurements. *IEEE J. Oceanic. Eng.* **30**, 153–164 (2005).
12. Ledlie, J. *et al.* Molé: a scalable, user-generated WiFi positioning engine. *J. Locat. Based Serv.* **6**, 55-80 (2012).
13. Alexander, J. & Rusvik, N. Localizing Cell Towers from Crowdsourced Measurements (2015). Retrieved from
https://wiki.opencellid.org/images/e/ea/Localizing_Cell_Towers_from_Crowdsourced_Measurements_-_Johan_Alexander_Nordstrand_-_Master_Thesis.pdf.
14. Manandhar, D. *et al.* Results of IMES (Indoor Messaging System) Implementation for Seamless Indoor Navigation and Social Infrastructure Platform (2010). Retrieved from https://www.gnss.co.jp/wp-content/uploads/2015/03/p74_Manandhar_SessionF2_ION2010_11.pdf.
15. Manna, K. *et al.* Evaluation of Multi-Sensor Fusion Methods for Ultrasonic Indoor Positioning. *Appl. Sci.* **11**, 6805 (2021).
16. Matsubara, G. *et al.* Positioning System for Subway Lines and Stations Using Cellular Tower IDs (2017). Retrieved from <http://www.ipin2017.org/ipinpapers/202/202.pdf>.
17. Khedr, M. & El-Sheimy, N. S-PDR: SBAUPT-Based Pedestrian Dead Reckoning Algorithm for Free-Moving Handheld Devices. *Geomatics* **1**, 148–176 (2021). <https://doi.org/10.3390/geomatics1020010>.

18. Hyuga, S. et al. Estimate a User's Location Using Smartphone's Barometer on a Subway (2015). Retrieved from <http://citeseerx.ist.psu.edu/viewdoc/download?doi=10.1.1.1068.2227&rep=rep1&type=pdf>.
19. Tanaka, H.K.M. Muometric positioning system (μ PS) with cosmic muons as a new underwater and underground positioning technique. *Sci. Rep.* **10**, 18896 (2020). <https://doi.org/10.1038/s41598-020-75843-7>
20. Hambling, D. Cosmic rays used for Arctic GPS. *New Sci.* **252**, 8 (2021). [https://doi.org/10.1016/S0262-4079\(21\)02186-2](https://doi.org/10.1016/S0262-4079(21)02186-2)
21. Tanaka, H. K. M. et al. High resolution imaging in the inhomogeneous crust with cosmic-ray muon radiography: the density structure below the volcanic crater floor of Mt. Asama, Japan. *Earth Planet. Sci. Lett.* **263**, 104113 (2007).
22. Tanaka, H. K. M. et al. Imaging the conduit size of the dome with cosmic-ray muons: The structure beneath Showa-Shinzan Lava Dome, Japan. *Geophys. Res. Lett.* **34**, 053007 (2007).
23. Tanaka, H. K. M., Uchida, T., Tanaka, M., Shinohara, H. & Taira, H. Cosmic-ray muon imaging of magma in a conduit: Degassing process of Satsuma-Iwojima Volcano, Japan. *Geophys. Res. Lett.* **36**, L01304 (2009).
24. Tanaka, H. K. M., Kusagaya, T. & Shinohara, H. Radiographic visualization of magma dynamics in an erupting volcano. *Nat. Commun.* **5**, 3381 (2014).
25. Tanaka, H. K. M. Muographic mapping of the subsurface density structures in Miura, Boso and Izu peninsulas, Japan. *Sci. Rep.* **5**, 8305 (2015).
26. Tanaka, H. K. M. Instant snapshot of the internal structure of Unzen lava dome, Japan with airborne muography. *Sci. Rep.* **6**, 39741 (2016).
27. Olah, L., Tanaka, H. K. M., Ohminato, T. & Varga, D. High-definition and low-noise muography of the Sakurajima volcano with gaseous tracking detectors. *Sci. Rep.* **8**, 3207 (2018).
28. Jourde, K. et al. Muon dynamic radiography of density changes induced by hydrothermal activity at the La Soufrière of Guadeloupe volcano. *Sci. Rep.* **6**, 33406 (2016).
29. Tioukov, V. et al. First muography of Stromboli volcano. *Sci. Rep.* **9**, 6695 (2019).
30. Morishima, K. et al. Discovery of a big void in Khufu's Pyramid by observation of cosmic-ray muons. *Nature* **552**, 386–390 (2017).
31. Saracino, G. et al. Imaging of underground cavities with cosmic-ray muons from observations at Mt. Echia (Naples). *Sci. Rep.* **7**, 1181 (2017).
32. Cimmino, L. et al. 3D Muography for the Search of Hidden Cavities. *Sci. Rep.* **9**, 2974 (2019).
33. Frederic, L. et al. A new kind of view for a Double oven Crystal Oscillator, (2007). Retrieved from <https://ieeexplore.ieee.org/document/4319182>
34. von Watzdorf, S. & Michahelles, F. Accuracy of positioning data on smartphones (2010). Retrieved from <https://dl.acm.org/doi/10.1145/1899662.1899664>
35. Zandbergen, P. A. Accuracy of iPhone locations: a comparison of assisted GPS, WiFi and cellular positioning. *Trans GIS.* **13**, 5–26 (2009).

36. Garnett, R. & Stewart, R. Comparison of GPS units and mobile Apple GPS capabilities in an urban landscape. *Cartogr. Geogr. Inf. Sci.* **42**, 1–8 (2015).
37. Allkofer, O.C. *et al.* Cosmic ray muon spectra at sea-level up to 10 TeV. *Nucl. Phys. B* **259**, 1-18 (1985).
38. Jokisch, H. *et al.* Cosmic-ray muon spectrum up to 1 TeV at 75° zenith angle. *Phys. Rev. D* **19**, 1368 (1979).
39. Achard, P. *et al.* Measurement of the atmospheric muon spectrum from 20 to 3000 GeV. *Phys. Lett. B* **598**, 15-32 (2004).
40. Groom, D. E. *et al.* Muon stopping-power and range tables: 10 MeV–100 TeV. *At. Data Nucl. Data Tables* **78**, 183–356 (2001).
41. Raab, F. H. & Joughin, I. R. Signal processing for through-the-earth radio communication. *IEEE Trans. Commun.* **43**, 2995–3003 (1995). doi:10.1109/26.477502.
42. Signori, A. *et al.* Data Gathering from a Multimodal Dense Underwater Acoustic Sensor Network Deployed in Shallow Fresh Water Scenarios. *J. Sens. Actuator Netw.* **8**, 55. DOI:10.3390/jsan8040055.
43. Mahmood, A. *et al.* Time Synchronization in 5G Wireless Edge: Requirements and Solutions for Critical-MTC. *IEEE Commun. Mag.* **57**, 45-51 (2019). DOI: 10.1109/MCOM.001.1900379
44. Shi *et al.* Evaluating the Performance of Over-the-Air Time Synchronization for 5G and TSN Integration (2021). Retrieved from <https://arxiv.org/abs/2104.13873>.
45. Hiyama, M. *et al.* Implementation of precision clock synchronization protocol to IEEE802.11 (2009). Retrieved from https://ipsj.ixsq.nii.ac.jp/ej/?action=repository_action_common_download&item_id=61816&item_no=1&attribute_id=1&file_no=1
46. Milevsky, A. *et al.* Development and test of IEEE 1588 Precision Timing Protocol for ocean observatory networks. *OCEANS 2008*, 10734674 (2008). DOI: 10.1109/OCEANS.2008.5152029.
47. IEEE 802.1 Time-Sensitive Networking (TSN) Task Group (2021). Retrieved from <http://www.ieee802.org/1/pages/tsn.html>.
48. Cavalcanti, D. *et al.* Extending Accurate Time Distribution and Timeliness Capabilities Over the Air to Enable Future Wireless Industrial Automation Systems. *Proc. IEEE*, **107**, 1132–1152, (2019).
49. Ajaz, A. High-Performance Industrial Wireless: Achieving Reliable and Deterministic Connectivity Over IEEE 802.11 WLANs. *IEEE open j. Ind. Electron. Soc.* **1**, 28–37 (2020).

Figures

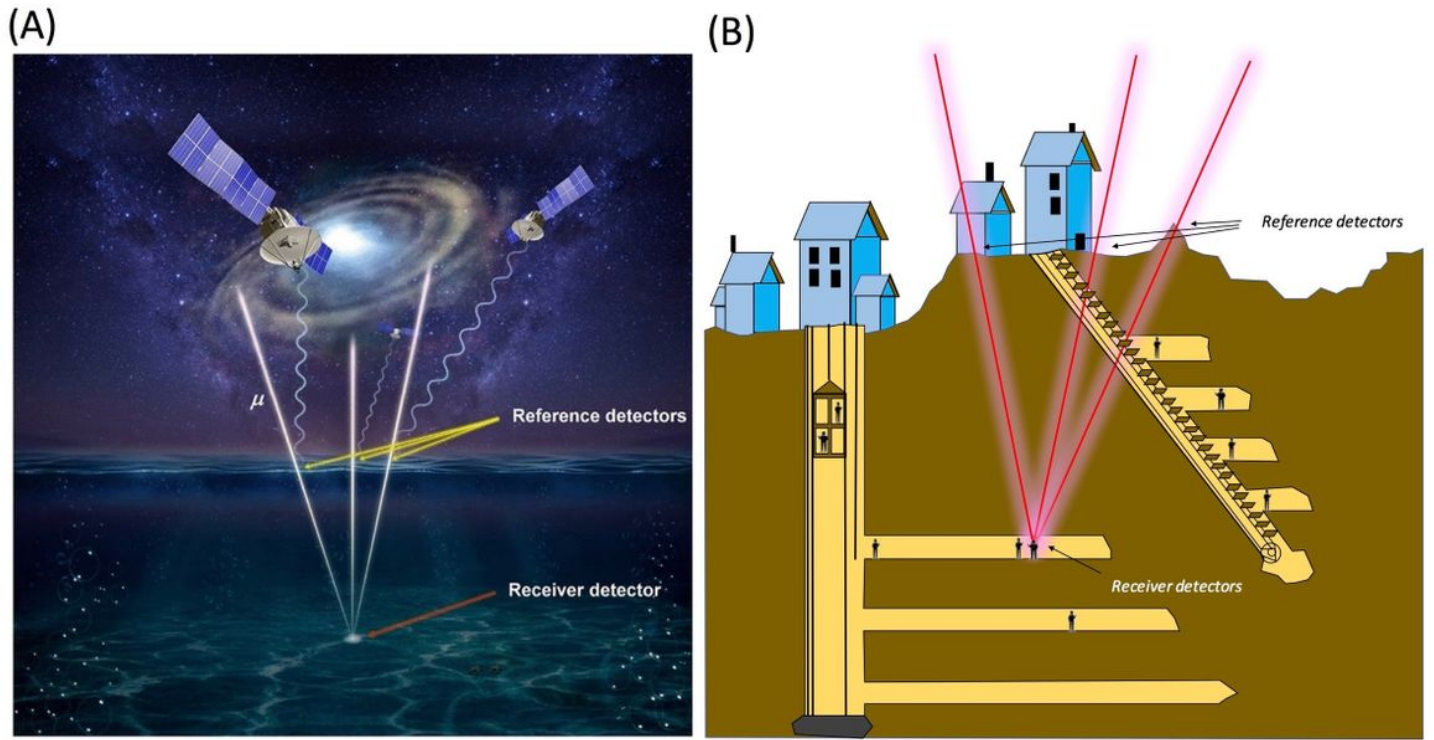


Figure 1

Principle of muPS. For underwater navigation, multiple reference detectors are located on the sea surface to navigate underwater receivers (A), and for underground navigation, multiple reference detectors are located on the ground surface to navigate underground receiver (B). The red lines indicate the muon trajectories. The copyright of these image is owned by HKMT.

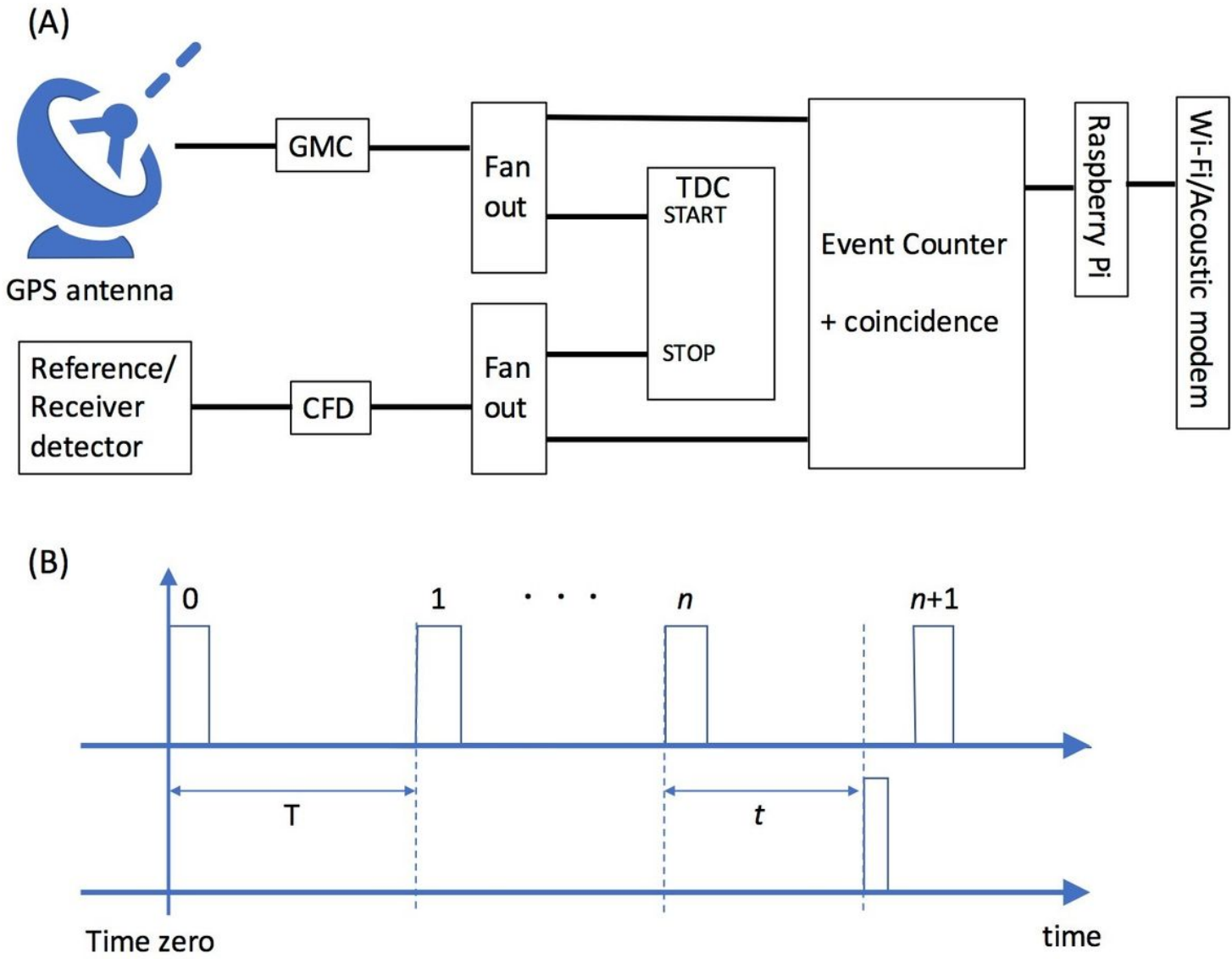


Figure 2

Block diagram of the current wireless muometric positioning/navigation system (MuWMS) (A). Both reference detectors and receiver detectors are initially connected with a GPS antenna, but the receiver detectors will be eventually disconnected from the GPS signals when entering indoor/underground/underwater regions. The principle to define the time after the GPS signals are lost is illustrated in (B). "Time zero" indicates the moment when the GPS signals are lost. T is the GMC signal output period that usually ranges from 10 to 100 ns. t is the time difference between the GMC signal pulse input and the MuWNS signal pulse input.

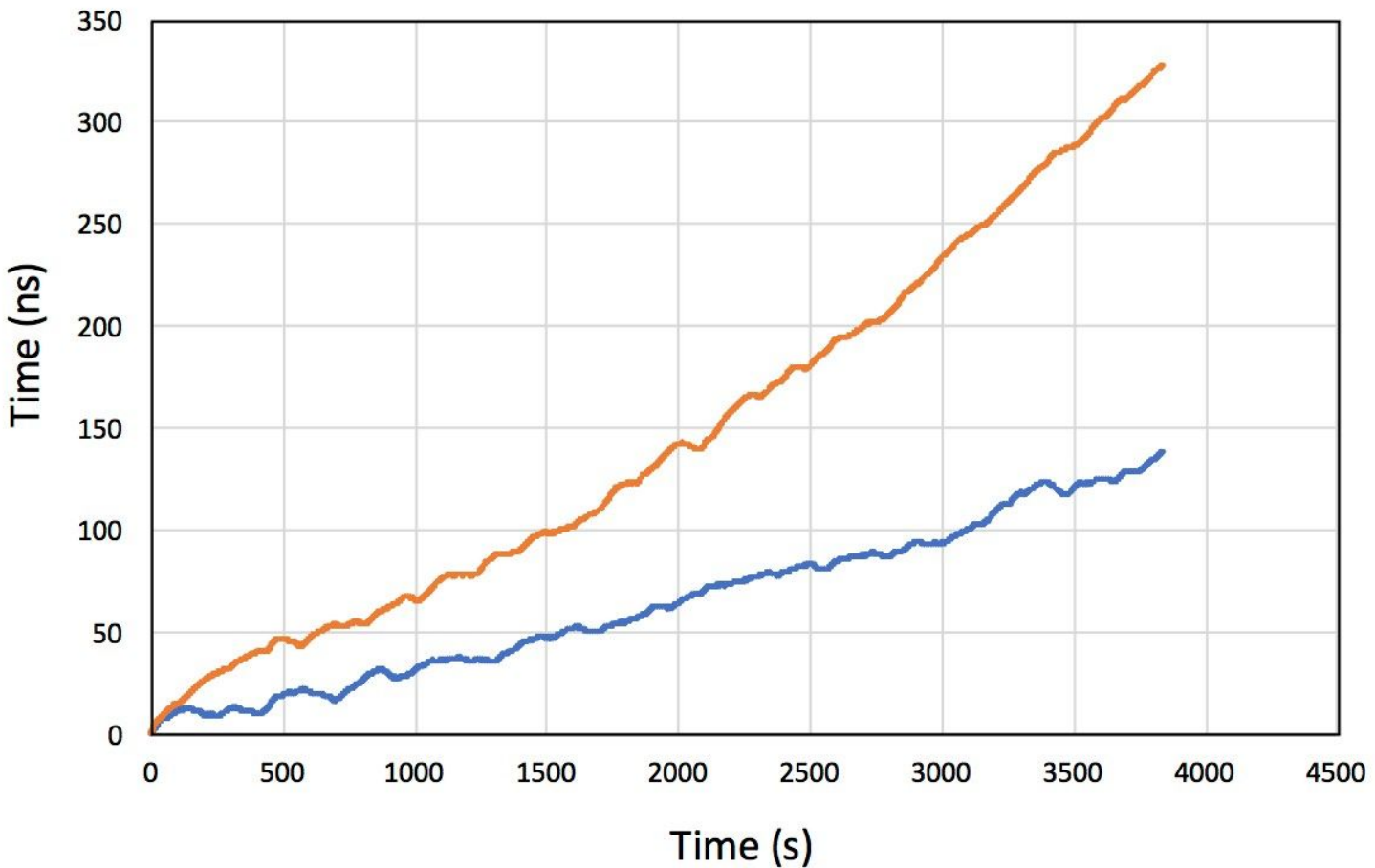


Figure 3

Averaged current OCXO time offset ($\langle \Delta t \rangle$) (blue lines) and the standard deviation (SD) of Δt ($\sigma(t)$) (orange lines) as a function of time.

Figure 4

Measurement accuracy ($c_0 \sigma(t)$) as a function of the maximum distance between the reference and receiver detectors for various muon arrival angles from horizon (green: 100 mrad; sky blue: 150 mrad; yellow: 200 mrad; gray: 250 mrad; red: 300 mrad; and blue: 350 mrad).

Figure 5

Time-dependent standard deviation (SD) of Δt ($\sigma(t)$) averaged over single (blue lines), double (orange lines) and triple (gray lines) OCXO outputs.

Figure 6

Schematic view of the Toranomon Hills Station Tower (THST) complex (A). The top view of the complex is shown in (B). The a-b line indicates the intersectional line of the cross-sectional view shown in A. The red lines indicate the underground space of the complex. The red and blue filled circles respectively indicate the position of "A" and "B" used for the discussion in the main text. The corresponding soil/concrete thickness distributions are respectively shown in (C) and (D). The copyright of this image is owned by HKMT.

Figure 7

Side (A), inside photograph (B) and top views (C, D, and E) of Akiyoshido cave. The dashed line indicates the actual geometry of the cave, but a cylindrical cave (empty near horizontal space underneath the overburden) was assumed in this work (A). In the top views, the locations of the reference detectors (blue filled squares) and receiver detectors (red filled squares) are shown. The cave region is indicated by the region filled in with darker blue. The locations of the reference detectors (blue filled squares) and receiver detectors (red filled squares) are also shown. Blue filled circles indicate the region within 150 m from the receiver detector. The double lines and the labels "P" respectively indicate roads and parking lots. The contour lines showing elevations are also shown. HKMT took the photograph. HKMT drew the map and the image with Microsoft PowerPoint software and holds the copyright.

Figure 8

Time required for recording one muon track as a function of rock thickness for various muon arrival angles from horizon (from top to bottom - sky blue: 500 mrad; yellow: 450 mrad; gray: 400 mrad; red: 350 mrad; and blue: 300 mrad) (A) and the corresponding $c_0\sigma$ (B).

Figure 9

Conceptual view of the undersea MuWNS in conjunction with the Robotic Vessels as-a-Service (RoboVaaS) (A). Yellow panels on the Unmanned Surface Vehicles (USVs) indicate the reference detectors to navigate an Unmanned Underwater Vehicle (UUV). The red line indicates the muon trajectory. The c_0 s as a function of the muon arrival angles from the horizon is also shown (B). The copyright of this image is owned by HKMT.